


## Article

# Endoscopic OCT Angiography Using Clinical Proximal-End Scanning Catheters

Lin Yao <sup>1</sup>, Yuan Zhou <sup>2</sup>, Kaiyuan Liu <sup>1</sup>, Xiaoting Yin <sup>1</sup>, Xiaofeng Deng <sup>1</sup>, Zhihua Ding <sup>1</sup> and Peng Li <sup>1,3,4,\*</sup>

<sup>1</sup> State Key Lab of Modern Optical Instrumentation, College of Optical Science and Engineering, Zhejiang University, Hangzhou 310027, China; yaolin@zju.edu.cn (L.Y.); lky528@zju.edu.cn (K.L.); 12130044@zju.edu.cn (X.Y.); dengxf@zju.edu.cn (X.D.); zh\_ding@zju.edu.cn (Z.D.)

<sup>2</sup> Department of Vascular Surgery, Sir Run Run Shaw Hospital, Zhejiang University School of Medicine, Hangzhou 310020, China; 3319027@zju.edu.cn

<sup>3</sup> Jiaxing Key Laboratory of Photonic Sensing & Intelligent Imaging, Jiaxing 314000, China

<sup>4</sup> Intelligent Optics & Photonics Research Center, Jiaxing Research Institute, Zhejiang University, Jiaxing 314000, China

\* Correspondence: peng\_li@zju.edu.cn

**Abstract:** Endoscopic optical coherence tomography angiography (OCTA) is a promising modality to inspect the microvasculature of inner organs in the early-stage tumor diagnosis. However, an endoscopic clinical proximal-end scanning catheter has limited flow imaging capability due to the nonuniform rotational distortion (NURD) and physiological motion. In this study, a combined local and global (CLG) optical flow algorithm was used to estimate the motion vectors caused by NURD and physiological motion. The motion vectors were used to bicubic-interpolation-resample the OCT structure to ensure that the circumferential pixels were equally spaced in the space domain. Then, angiograms were computed based on the statistical relation between inverse SNR (iSNR) and amplitude decorrelation (IDa), termed as IDa-OCTA. Finally, the ability of this technique for endoscopic OCTA imaging was demonstrated by flow phantom experiments and human nailfold capillary imaging.



**Citation:** Yao, L.; Zhou, Y.; Liu, K.; Yin, X.; Deng, X.; Ding, Z.; Li, P. Endoscopic OCT Angiography Using Clinical Proximal-End Scanning Catheters. *Photonics* **2022**, *9*, 329. <https://doi.org/10.3390/photonics9050329>

Received: 10 April 2022

Accepted: 9 May 2022

Published: 10 May 2022

**Publisher's Note:** MDPI stays neutral with regard to jurisdictional claims in published maps and institutional affiliations.



**Copyright:** © 2022 by the authors. Licensee MDPI, Basel, Switzerland. This article is an open access article distributed under the terms and conditions of the Creative Commons Attribution (CC BY) license (<https://creativecommons.org/licenses/by/4.0/>).

**Keywords:** biomedical imaging; clinical proximal-end scanning catheters; endoscopic optical coherence tomography angiography

## 1. Introduction

Angiogenesis is closely associated with tumor growth, invasion, and spread [1]. Narrow-band imaging (NBI) [2] and confocal laser endomicroscopy (CLE) [3] have been used for investigating microvascular changes as hallmarks of early-stage cancer. However, NBI only enables superficial vasculature visualization with limited resolution, whereas CLE only has a relatively small field of view (FOV) with the requirement of exogenous contrast agents. As a functional extension of optical coherence tomography (OCT), OCT angiography (OCTA) can rapidly visualize the subsurface three-dimensional (3D) microvasculature down to the capillary level in a label-free manner by utilizing the motion contrast of red blood cells (RBCs) [4–6], and has been used to evaluate the tumor vessels in ophthalmology [7–9]. In addition, endoscopic OCTA has been proposed in the early-stage cancer diagnosis of inner organs such as Barrett's esophagus (BE) [10,11]. However, OCTA images of high quality require a stable beam scanning, which makes it a challenge for miniature probes.

A variety of scanning mechanisms have been proposed to realize endoscopic OCTA imaging. Wurster et al. used a tubular piezoelectric actuator to generate two-dimensional (2D) spiral scanning with a 1.3 mm diameter circular FOV at the focal plane, where the diameter of the probe was 4 mm [12]. However, in the spiral scanning pattern, because of the sequential circular scans with different radial distance and spatial sampling, additional

decorrelation noise artifacts might be produced in the inter-frame (circles) OCTA [12]. In addition, the spiral scans are inefficient in sampling toward the circular center, and frequent trajectory calibration is required due to amplitude-dependent phase variation in the piezoelectric fiber scanner. Yao et al. used an electrothermal micro-electro-mechanical system (MEMS)-based probe with a diameter of 3.5 mm to generate a stable and controllable raster scanning pattern with a 2 mm × 2.3 mm FOV at the distal end, suppressing the decorrelation noise caused by spatial mismatch between paired scans [13]. However, the small FOV of spiral and raster scanning patterns might be inefficient for large-scale inspecting lesions of inner organs.

To meet the requirement of large-scale inspection, side-viewing circumferential scanners are a natural choice, including distal-end scanning and proximal-end scanning. Micromotors have been used for distal-end scanning, whose speed can be up to 4000 revolutions per second (rps) [14]. Fujimoto et al. used a micromotor-based distal-scanning probe with a diameter of 3.2 mm to realize angiographic imaging of the esophagus in vivo [10,11,15–18]. In addition, Fujimoto et al. also designed a micromotor-based capsule probe with a diameter of 12 mm for rectal angiographic imaging [17,19]. However, due to the existence of micromotors, the size of distal-end scanning probes is relatively large and the expense is high, limiting the clinical application such as pancreaticobiliary strictures.

In contrast to the distal-end scanners, the proximal-end scanning probes up to 200 rps rely on the long torque coil to transmit the proximal rotation to the imaging optics at the distal tip; thus, they are more economical, compact, and commercially available [14]. However, clinical proximal-end scanning catheters have limited flow imaging capability due to the artifacts from the nonuniform rotational distortion (NURD) caused by the mechanical friction between the catheter sheath and torque coil [20], and physiological motion such as heartbeat and breathing [21]. In the known literature, only Joseph et al. used the clinical proximal-end scanning catheter with a diameter of 0.9 mm to image a dynamic flow, based on statistical analysis of the cross-correlation between sequential frames to generate a flow mask [20,22]. However, the statistical analysis method requires 30 cross correlation maps to ensure its classification accuracy, and oversampling affects imaging speed.

To correct the artifacts in OCT catheters-based systems, Fujimoto et al. proposed a correction method using the fiducial markers on the catheter to correct rotational speed variations, but it induced an obstructed FOV and could not correct physiological motion [18]. Kang et al. used the local block motion (LBM) method to determine the motion locally by estimating the translation between corresponding blocks of adjacent frames, but the execution time of it was slow, consuming 15 s to process one cross-sectional image [23]. When the fiducial markers method was extended to be combined with the LBM method, using the tissue feature as the fiducial markers could correct the physiological motion artifacts [24]. Uribe-Patarroyo et al. developed a method based on the statistical variations of speckle between adjacent A-lines to measure the rotational speed of a catheter, but it required highly correlated A-lines data limiting the imaging speed [25]. The optical flow method based on the tissue intensity constant assumption between adjacent frames for tracking motion is able to acquire the flow field information for each pixel with a sub-pixel precision, achieving high accuracy with fast execution time [26,27].

In this work, we proposed an endoscopic OCTA using a clinical proximal-end scanning catheter with a diameter of 0.9 mm. First, we introduced a combined local and global (CLG) optical flow model to correct artifacts of the OCT original structures, including NURD and physiological motion. Secondly, we validated the method through flow phantom experiments. In angiograms before and after correction, the distortion-induced noise was removed well, and the overlap state of the dynamic and static voxels in the inverse SNR and amplitude decorrelation (IDa) space was significantly improved. Then, we conducted human nailfold capillary imaging, and compared the endoscopic OCTA results with the conventional OCTA results using a galvanometric scanner, achieving good correspondence. Finally, the potential applications and limitations of this study were discussed.

## 2. Methods

### 2.1. System Setup

Figure 1 shows the schematic diagram of swept-source OCTA (SS-OCTA) systems using the endoscopic clinical proximal-end scanning catheter and conventional galvanometric scanner. The laser centered at 1300 nm operates at a 100 kHz sweeping rate over a  $\sim 100$  nm spectral bandwidth, providing an experimental axial resolution of  $\sim 16$   $\mu\text{m}$  and an imaging range of  $\sim 11$  mm in the air. The basis of the SS-OCTA system was an interferometer, where the light from the laser source was split into the sample arm and the reference arm by a 90:10 fiber coupler. As shown in Figure 1a, the sample arm was terminated in a clinical proximal-end scanning catheter (St Jude Inc., St. Paul, Minnesota, USA, C7 Dragonfly), which allowed light to be transmitted to and collected from the sample, offering an experimental lateral resolution of  $\sim 25$   $\mu\text{m}$  and a working distance of  $\sim 1.5$  mm [28]. The catheter was 0.9 mm in diameter and encapsulated all material in a transparent plastic sheath, and was in connection with the OCT interferometer by the optical connector (Princetel Inc., Trenton, NJ, USA, MJXA-SAPB-131-28-025-FA). A motor (maxon, Suzhou, China, EC-max30) was used to rotate the catheter for circumferential scanning while maintaining optical connection. As shown in Figure 1b, in the OCT sample arm, a scanning lens (Thorlabs, Newton, NJ, USA, LSM05) with an effective focal length of 54 mm was used collimate the detecting light on the sample, providing an experimental lateral resolution of  $\sim 32$   $\mu\text{m}$ , and an x-y galvanometer was adopted for 3D volume scanning. The light backscattered from the sample was recombined with the light reflected from the reference mirror, and then the interference signal was detected by a balanced detector (Thorlabs, Newton, NJ, USA, PDB470C).

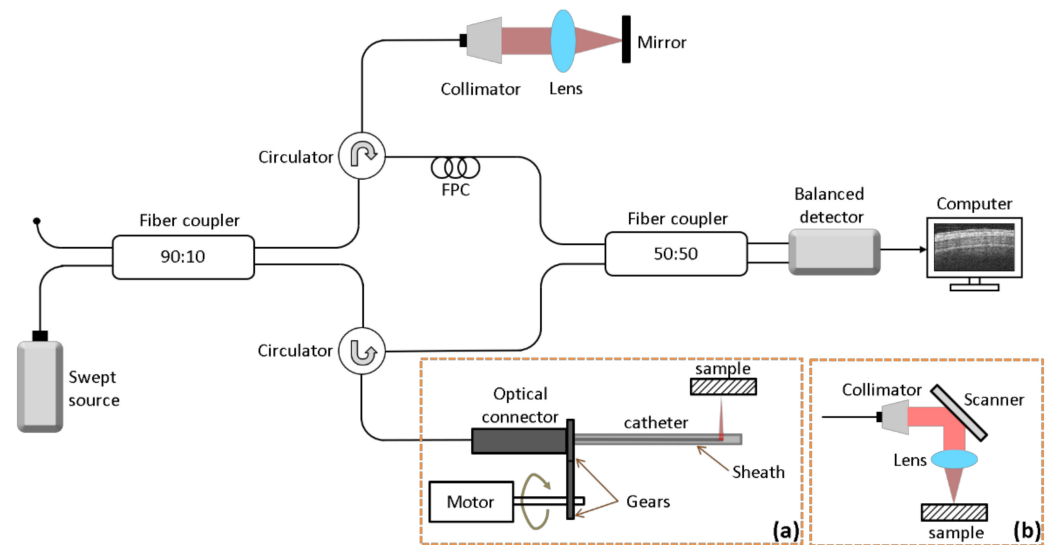


**Figure 1.** Schematic of the SS-OCT system setup where the sample arm is terminated with a clinical endoscopic proximal-end scanning catheter (a) and a conventional galvanometric scanner (b). FPC: fiber polarization controller.

In the imaging experiments with a clinical endoscopic proximal-end scanner, the motor rotary speed (imaging speed) was set to 25 rps (up to 134 rps), and each dataset contained 5 frames with 4002 A-lines per frame, where the axial pixel size was  $\sim 8$   $\mu\text{m}$  and the lateral pixel size was  $\sim 2.5$   $\mu\text{m}$ . When using a conventional galvanometric scanner, the imaging speed was set to 156 Hz, and each dataset contained 5 frames with 512 A-lines per frame. This study was conducted in accordance with the Declaration of Helsinki (as revised in 2013). This study was approved by the Ethics Committee of Zhejiang University (No.: IRB-2021-461) and the informed consent was obtained from subjects before imaging.

### 2.2. Distortion Correction

Optical flow is the apparent movement of brightness patterns in an image over time. The classic optical flow method relies on the brightness constant assumption (BCA) [26], which assumes the image brightness of a target pixel remaining constant over time. In the OCT images, the BCA can be expressed as:

$$I(z, x, t) = I(z + dz, x + dx, t + dt) \tag{1}$$

where  $I$  is the OCT signal intensity,  $z$  is the radial (deep) index,  $x$  is the circumferential index, and  $t$  is the temporal index. The spatial position  $(z, x)$  is located in the OCT static regions of interest (ROIs) to avoid the intensity change of the dynamic flow affecting the application of the optical flow method.

According to Equation (1), by applying a first-order Taylor expansion, the linear approximation termed as the optical flow constraint (OFC) can be defined as follows:

$$I_z u + I_x v + I_t = 0 \tag{2}$$

where  $u = \frac{dz}{dt}$  and  $v = \frac{dx}{dt}$  denote image motion at position  $(z, x)$ ,  $I_z$  and  $I_x$  are gradient vectors of the OCT intensity values, and  $I_t$  is the temporal intensity variation at position  $(z, x)$ . Equation (2) cannot be solved for both  $u$  and  $v$  in every single pixel, and an additional constraint is needed. One widely used is a global method called Horn–Schunk (HS), which assumes smoothness of the flow in the whole image and introduces a global smoothness constraint [26]. Another one is a local method called Lucas–Kanade (LK), which assumes the flow to be approximately constant within a local neighborhood of the given pixel [29]. Here, a combined local and global (CLG) method was used, involving both local (LK) and global (HS) optical flow methods [30,31]:

$$E(u, v) = \iint_R [\Psi((I_z u + I_x v + I_t)^2) + \alpha \Psi(|\nabla u|_2 + |\nabla v|_2)] dz dx \tag{3}$$

where  $R$  denotes a local window in a static ROI.  $\Psi(s^2) = \sqrt{s^2 + \epsilon^2}$  is an increasing concave function, where  $\epsilon$  is set to a small positive constant 0.001 that ensures  $\Psi(s)$  is still convex, offering advantages in the minimization process.  $\nabla$  is the gradient operator.  $\alpha$  set to 0.012 is the smoothness weight factor (regularization parameter). Then, a three-level coarse-to-fine multiscale approach with a downsampling ratio of 0.5 [30] was used to solve the motion vectors  $(u, v)$ , minimizing the energy  $E(u, v)$ , and a  $20 \times 20$  window size was used for the local smoothing process.

In addition, the structural similarity index (SSIM) was used to evaluate the similarity between the two OCT images, which was based on luminance ( $I$ ), contrast ( $c$ ), and structure ( $s$ ) [32]:

$$SSIM = [I(I_1, I_2)^\alpha \cdot c(I_1, I_2)^\beta \cdot s(I_1, I_2)^\gamma] \tag{4}$$

$$I(I_1, I_2) = \frac{2\mu_{I_1}\mu_{I_2} + C_1}{\mu_{I_1}^2 + \mu_{I_2}^2 + C_1}, c(I_1, I_2) = \frac{2\sigma_{I_1}\sigma_{I_2} + C_2}{\sigma_{I_1}^2 + \sigma_{I_2}^2 + C_2}, s(I_1, I_2) = \frac{\sigma_{I_1 I_2} + C_3}{\sigma_{I_1}\sigma_{I_2} + C_3} \tag{5}$$

where  $(\mu_{I_1}, \mu_{I_2})$ ,  $(\sigma_{I_1}, \sigma_{I_2})$ , and  $\sigma_{I_1 I_2}$  are the local means, standard deviation, and cross-covariances of OCT images  $I_1$  and  $I_2$ , respectively.  $\alpha$ ,  $\beta$ , and  $\gamma$  set to 1 here are weight factors.  $C_1$ ,  $C_2$ , and  $C_3$  as nonnegative real numbers are regularization constants for  $I$ ,  $c$ , and  $s$  terms.

Figure 2 illustrates the number of iterations in each multiscale level for a recursive optical flow estimation in the phantom experiment, and the best SSIM (0.7039) was observed with 15 iterations, corresponding to a ~2 times improvement compared with the original SSIM (0.2199) with 0 iterations.

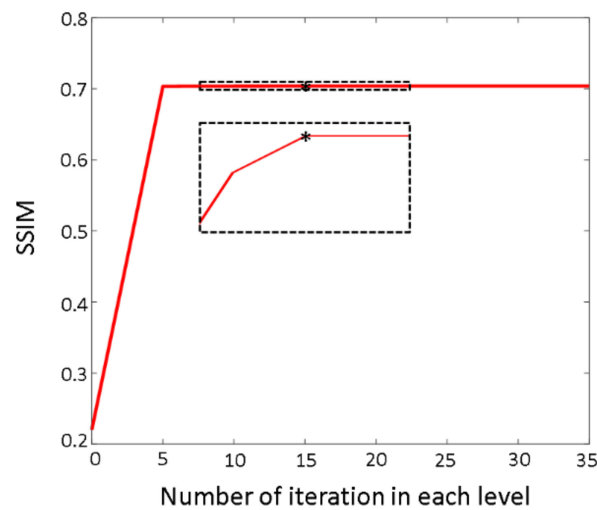


**Figure 2.** The SSIM for a different number of iterations in each multiscale level in phantom experiment. The inset is an enlarged view of the dashed box region. “\*” labels the best SSIM (0.7039) when 15 iterations.

The framework of the CLG optical flow method for distortion correction is summarized in the pseudo-code shown in Table 1. First, the static ROI (solid gel in upper layers of phantom, avascular epidermis of human skin or mucosa) was selected manually for optical flow estimation, avoiding the flow signals being misleading. Second, the CLG optical flow method was used to estimate the motion vectors  $(u, v)$  of pixels in the static ROI. Considering the 100 kHz rapid sweeping rate of the swept source, the motion vectors  $(u, v)$  of the pixels in one A-line were very similar, which could be averaged  $(u', v')$ . Finally, a bicubic spline resampling was applied to the OCT structure for correcting the NURD and physiological motion.

**Table 1.** Framework of the CLG distortion correction.

---

Input:
OCT intensity image $I$
Output:
OCT distortion corrected intensity image $I'$
1: Manually select static ROI in $I$ ;
2: for multiscale level $L = 1, 2, 3$ with downsampling ratio 0.5 do
3: for iteration $k = 1, 2, \dots, 15$ do
4: Solve for motion variable $(u_k, v_k)$ using CLG method with 0.012 regularization parameter and $20 \times 20$ window size;
5: end for;
6: Solve for motion variable $(u_{kL}, v_{kL})$ using $(u_{k=15}, v_{k=15})$ as initialization on this level;
7: end for;
8: Use the final solution $(u_{k=15, L=3}, v_{k=15, L=3})$ as motion vectors $(u, v)$ ;
9: Calculate the averaged motion vectors $(u', v')$ of same A-line;
10: Resample $I$ by bicubic interpolation;

---

### 2.3. IDa-OCTA Algorithm

To avoid the unstable phase problem in the SS-OCT system and suppress the random noise-induced decorrelation artifacts, a signal-to-noise (SNR) adaptive OCTA algorithm was used, which was based on the asymptotic relation between inverse SNR (iSNR) and amplitude decorrelation, termed as IDa-OCTA [13]. The OCTA motion contrast was

computed using the inter-frame amplitude decorrelation  $D$  with a spatio-temporal kernel (window size for decorrelation calculation) [13]:

$$D = 1 - \frac{C}{I} = 1 - \frac{\sum_{m=1}^M \sum_{t=1}^{T-1} x_0(m, t)x_0(m, t + 1)}{\sum_{m=1}^M \sum_{t=1}^{T-1} \frac{x_0^2(m, t) + x_0^2(m, t+1)}{2}} \tag{6}$$

where  $x_0(m, t)$  denotes the normalized amplitude of the OCT signal,  $C$  is the local first-order auto-covariance, and  $I$  is the local zeroth-order auto-covariance, meaning the intensity. Here,  $m$  is the spatial index to denote  $(z, x)$  and  $M$  is the total kernel size in spatial dimensions,  $t$  is the temporal index, and  $T$  is the number of repeated frames at the same location. The saturation limit of the amplitude decorrelation  $D$  in dynamic regions was derived to be  $\sim 0.22$  [13].

The distribution area of static and noise voxels in the IDa space was predefined with the asymptote relation  $\overline{D}_{st}$  and an additional distribution variance  $3\sigma_{st}$  range. The range of  $3\sigma_{st}$  was set consistent with the previous OCTA studies [6,13], which had a great classification performance. The classification line  $D_c$  was described [13]:

$$D_c(iSNR) = \overline{D}_{st} + 3\sigma_{st} = \overline{D}_{st} + 3\sqrt{\frac{2}{N}}\sigma_{st0} \tag{7}$$

where  $\overline{D}_{st}$  and  $\sigma_{st}$  denote the mean value and the standard deviation (std) of amplitude decorrelation in static regions, respectively, mathematically derived based on the multivariate time series (MVTs) model [13].  $N = M \cdot T$  is the total spatio-temporal kernel size, and  $\sigma_{st0}$  is the std of amplitude decorrelation when  $T = 2$ . The variance of the IDa distribution is inversely proportional to the total kernel size  $N$ . As a tradeoff between the spatial resolution, imaging time, and classification performance, a practical spatio-temporal kernel of  $5 \times 3 \times 5$  ( $z \times x \times t$ ) was used to analyze flow phantom and human skin data, the corresponding axial resolution was blurred for 2.5 pixels ( $5/2 = 2.5$  axial resolution volumes in 5 pixels), and, at the same time, laterally, there were 3.3 overlapped scans ( $3/10 = 0.3$  lateral resolution volumes in 3 pixels) for a clear imaging in the circumferential direction. The IDa space can be divided into a dynamic part ( $D > D_c$ ) and static/noise part ( $D \leq D_c$ ). The dynamic voxels were labeled as 1 and the others were labeled as 0, and accordingly, the IDa vascular mask was generated. Finally, the IDa-OCTA angiograms were generated by multiplying the amplitude decorrelation map by the IDa mask.

To quantify the performance of the CLG-corrected IDa-OCTA, the contrast-to-noise ratio (CNR) was calculated [6]:

$$CNR = \frac{\overline{D}_{dy} - \overline{D}_n}{\sigma_n} \tag{8}$$

where  $\overline{D}_{dy}$  and  $\overline{D}_n$  denote the mean value of decorrelation in the dynamic flow and noise regions, respectively, and  $\sigma_n$  is the standard variance in the noise regions.

### 3. Results

The flow phantom model was used to demonstrate the correction effect of the distortion. The flow phantom was made of two parts: one was solid gel mixed with  $\sim 5\%$  milk to mimic the static tissue background, and the other part were capillary tubes with an inner diameter of  $0.3 \pm 0.1$  mm full of milk solution to mimic a dynamic flow. As shown in the cross-sectional structure, Figure 3a, six capillary tubes in total were embedded in the solid gel, distributing at different depths to simulate actual blood vessels with different SNRs (the lowest  $< 10$  dB). As shown in the IDa-OCTA before correction, Figure 3b, due to the distortion, the static region unusually presented a high decorrelation value similar to that of the dynamic flow. According to the classification line  $D_c$ , the IDa space can be separated into a static/noise part (labeled by light blue) and dynamic part (labeled by light red). In the corresponding IDa feature space of Figure 3b, the scatterplots of the static/noise (the dashed rectangles in Figure 3a) and dynamic (the solid rectangles in Figure 3a) voxels were

most overlapped and not in agreement with the predefined IDa space (see Figure 3e). Thus, it is a challenge to separate the static and dynamic regions using the IDa classification line. To solve the problem, the CLG correction method was performed on the cross-sectional structure. The advantage of the CLG method was demonstrated by comparing with the conventional LBM method [23] both qualitatively and quantitatively. After distortion correction, the distortion-induced noise in the static region of IDa-OCTA was removed to some extent (see Figure 3c,d). Comparing the two cross-sectional angiograms after CLG and LBM correction, the residual noise was more obvious in Figure 3d, highlighted by the cyan triangles. As shown in Figure 3f after correction, the scatterplots of the regions identical to Figure 3b were in good agreement with the predefined IDa space. The static voxels in the CLG-corrected image compared with those in the LBM-corrected image were better separated with dynamic voxels, meaning fewer misclassification voxels (residual noise) in IDa-OCTA (see the bold arrow in Figure 3f). To further quantify the improvement of the CLG method over the LBM method, a ground truth mask of dynamic flow was manually labeled. The histograms of angiograms in Figure 3c,d are plotted in Figure 3g,h, where the CLG-corrected angiogram obviously separates dynamic flows and background noise better, highlighted by the green bold arrow. According to Equation (5), the CNR of the CLG-corrected angiogram (6.45) is higher than that of the LBM-corrected angiogram (6.22), corresponding to a 3.70% improvement in dynamic contrast. In addition, the superior performance of the CLG correction method enables an improved accuracy of flow density quantification. A decorrelation threshold was applied to both the CLG-corrected angiogram and LBM-corrected angiogram to quantify the flow density [33], and the voxels above the threshold divided by the total voxels in the ROI defined the flow density. The manually labeled ground truth mask was used to calculate the relative error (RE) of the flow density, which means a difference between the estimated flow density and the ground truth. The RE of the CLG-corrected angiogram (1.44%) was significantly lower than that of the LBM-corrected angiogram (6.17%), corresponding to a 76.7% improvement in the quantification in flow density. In addition, the execution time of CLG correction (1.40 s) was significantly shorter than that of the LBM correction (13.16 s) between two sequential structural frames (in upper static solid gel regions,  $4002 \times 130$  pixels), with an order of magnitude improvement, which is consistent with past studies [23,27].

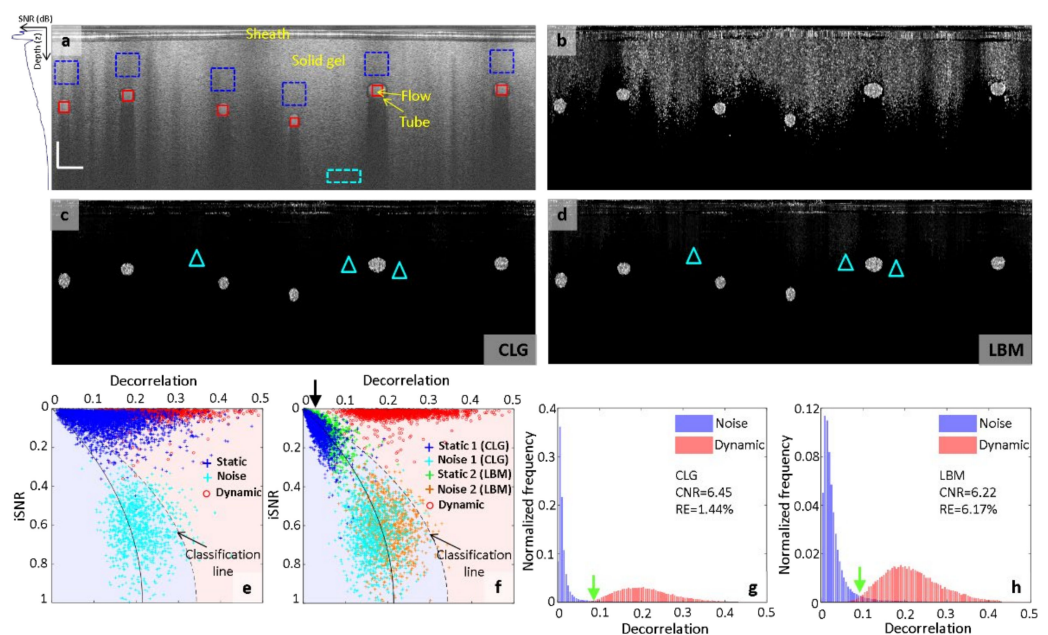


**Figure 3.** Validation of the correction effect of the distortion through flow phantom experiment imaging with endoscopic clinical proximal scanner. (a) Cross-sectional structure of flow phantom. Left inset is the averaged depth profile indicating the SNR decay. The mean iSNR and SNR of the deepest

flow region were approximately 0.09 and 10 dB, respectively. Cross-sectional IDa-OCTA angiograms before correction (b), after using CLG correction (c) and after using LBM correction (d). The residual noise was obvious in (d), highlighted by the cyan triangles. The scatterplots of the static (blue dashed rectangles in a), noise (cyan dashed rectangles in a) and dynamic (red solid rectangles in a) voxels in IDa space before (e) and after (f) distortion correction, and the solid and dashed lines correspond to the theoretical asymptotic IDa relation  $\overline{D_{st}}$  and the classification line  $D_c$ , respectively. Histograms of flow signals and background noise in CLG-corrected IDa-OCTA (g) and LBM-corrected IDa-OCTA (h). The overlap between the flow signals and background noise was highlighted by the green bold arrow. A kernel of  $5 \times 3 \times 5$  ( $z \times x \times t$ ) was adopted in IDa-OCTA calculation. Scale bar = 0.5 mm.

As the skin tissue around the nailfold region contains characteristic structures with rich blood perfusion, the little finger nailfold on the left hand of a healthy female volunteer was imaged with the endoscopic catheter and the conventional galvanometric scanner. In the endoscopic cross-sectional structure (Figure 4a), the epidermis (EP), dermis (DE), nail matrix (NM), nail root (NR), and nail beds (NB) layers were clearly differentiated. The blood vessels were supposed to be mainly distributed within the DE layer [34]. The endoscopic cross-sectional IDa-OCTA angiogram without distortion correction is shown in Figure 4b, where the dynamic flows in the DE layer were not distinguishable from the neighbor static tissue. For comparison, a galvanometric scanner was used to image a similar little finger nailfold region, and the conventional cross-sectional IDa-OCTA angiogram (Figure 4c) was obtained, where the blood vessels could be clearly identified from the background with a high contrast. After performing distortion correction on endoscopic structures, the corresponding CLG-corrected endoscopic IDa-OCTA (Figure 4d) and LBM-corrected endoscopic IDa-OCTA (Figure 4e) both enabled a relatively clear visualization of the blood perfusion within the high scattering skin tissue, and the endoscopic angiograms had a good correspondence with the conventional angiogram (see the yellow arrow in Figure 4c–e), demonstrating the reality of the dynamic flow obtained by the endoscopic proximal-end scanning catheter. Compared with the CLG-corrected angiogram, the LBM-corrected angiogram had a higher background noise and thus a lower image contrast, partly circled by yellow ellipses in the insets. In addition, the noisy background also impaired the vessel density evaluation. As shown in Figure 4f,g, the binarized vascular masks of CLG- and LBM-corrected angiograms (red) were overlaid on the structural image, and the CLG-corrected image showed less noisy points labeled by yellow ellipses, enabling a higher accuracy in vessel density evaluation.

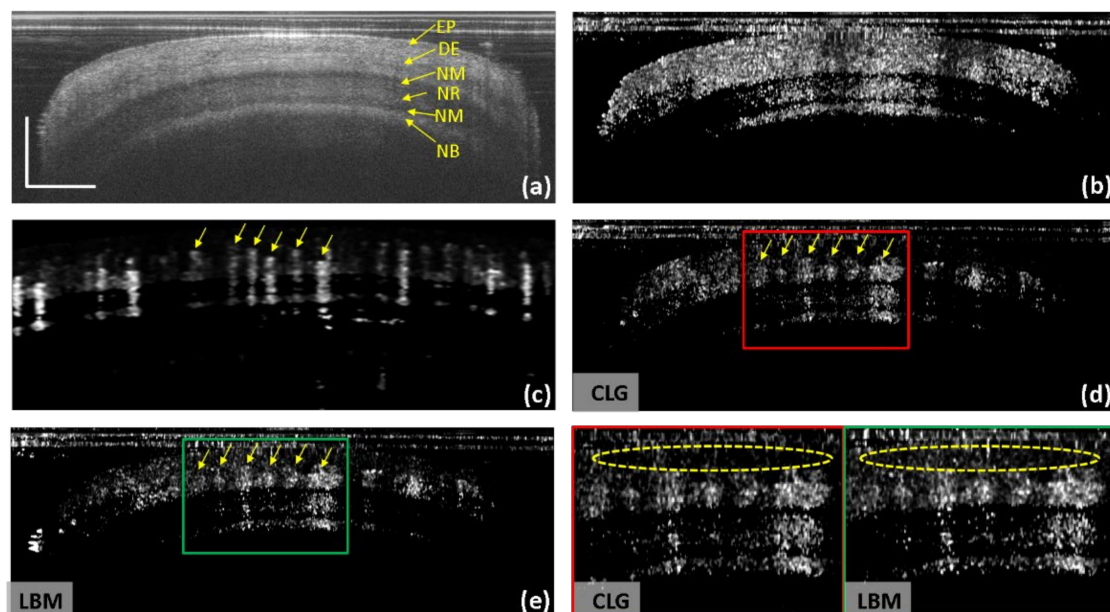
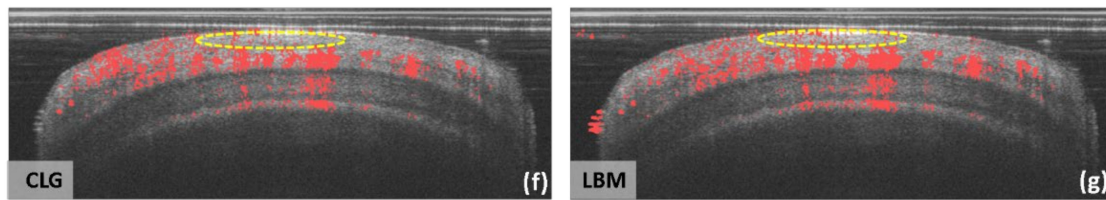


Figure 4. Cont.





**Figure 4.** IDa-OCTA imaging of the little finger nailfold of a healthy volunteer with the endoscopic clinical proximal-end scanning catheter and the conventional galvanometric scanner. (a) Endoscopic cross-sectional structure of the nailfold. (b) Endoscopic cross-sectional IDa-OCTA angiogram before correction. (c) Conventional cross-sectional IDa-OCTA angiogram obtained by imaging a similar nailfold position with a galvanometric scanner. Endoscopic cross-sectional IDa-OCTA angiogram after using CLG correction (d) and after using LBM correction (e). Left insets are enlarged views of the enclosed areas. Corresponding vessels are labeled by the yellow arrows. Overlay of the CLG-corrected endoscopic IDa-OCTA angiogram (red, (f)) and the LBM-corrected endoscopic IDa-OCTA angiogram (red, (g)) on the cross-sectional structure (gray). Corresponding residual noise is circled by yellow ellipses. EP: epidermis, DE: dermis, NM: nail matrix, NR: nail root, NB: nail bed. A kernel of  $5 \times 3 \times 5$  ( $z \times x \times t$ ) was adopted in IDa-OCTA calculation. Scale bar = 0.5 mm.

#### 4. Discussion

In this study, to suppress the distortion-induced noise of angiograms imaging with proximal-end scanning catheters, a CLG optical flow method was used to correct NURD and physiological motion. Flow phantom and human finger imaging experiments were performed to demonstrate its validity. The proposed distortion correction method has several advantages over existing methods. Compared with the conventional LBM method determining motion locally by estimating the translation between corresponding blocks of adjacent frames [23], the CLG optical flow method contains the flow field information available for each pixel, and estimates the circumferential ( $x$ ) and the radial ( $z$ ) displacements to sub-pixel precision, achieving higher accuracy with a significantly faster execution time [27]. In addition, rather than using the fiducial markers on the catheter to correct rotational speed variations [18], the CLG method ensures an unobstructed field of view. In contrast to the method based on the statistical variations in speckle between adjacent A-lines measuring the rotational speed of a catheter [25], the CLG method is based on the intensity constant assumption to calculate the velocity field from the adjacent frames, not requiring highly correlated A-lines data and not limiting the imaging speed. This distortion correction method can be applied to other endoscopic catheters-based techniques such as balloon-based distal-end probes for esophageal angiographic imaging [10,15–17], or capsule-based distal-end probes for rectal angiographic imaging [17,19]. In addition, it has potential to be combined with machine learning algorithms to further improve the performance of the CLG optical flow in distortion correction [35].

For endoscopic imaging, the vasculature signals are significantly important for the evaluation of benign and malignant diseases. In the malignant mucosa of inner organs, a large tumor burden may lead to profuse neovascularization, and accordingly, many tumor vessels are generated, always behaving as tortuous and abnormal dilated features [36]. In addition, due to the different degrees of tumor invasion depth from the epithelium to submucosa, the vascular phenotype shows different characteristics [1]. Compared with commonly using NBI and CLE to characterize vascular patterns, endoscopic OCTA imaging enables a subsurface image of inner organs with higher resolution than NBI, and allows a larger FOV than CLE without requirements of dye injection. Thus, endoscopic OCTA will be useful for the diagnosis of tumors of inner organs in the clinic. In addition, the clinical proximal-end scanning catheter we used has a diameter of 0.9 mm, and it can be easily inserted through commonly used esophagogastroduodenoscopy (EGD) endoscopes with a working channel of 2.8 mm [15]. In addition to the large tubular organs, it is also suitable for narrow lumen imaging such as pancreaticobiliary systems. In addition, the lateral resolution is mainly determined by the focal spot radius of the cylindrical gradient-index

(GRIN) lens. It can be improved by using a GRIN lens with a larger gradient constant or using a longer spacer to increase the distance between the GRIN lens and single-mode fiber (SMF), but at the expense of decreasing the working distance [37]. The current 25  $\mu\text{m}$  lateral resolution was chosen for a working distance of 1.5 mm, which can be improved to 18  $\mu\text{m}$  with a decreased working distance of 1.2 mm for a more detailed vascular visualization [37]. Considering that imaging of large lumens requires a long working distance such as the esophagus, a lateral resolution of 21  $\mu\text{m}$  and a long WD of 12 mm can be realized with a dual GRIN lens-based probe [38].

For bioimaging, improving the tissue contact coverage with the catheter will likely increase the robustness and the accuracy of the motion displacements estimation. In our human finger imaging experiments, the cross-sectional structural image used for motion displacements estimation only covered closely a portion of the finger nailfold, while the other tissue regions were out of contact. Dominant motion distortion requiring correction was in the circumferential direction. Radial motion where finger tissue was contact with the catheters was relatively small and the blood vessels can be identified from the background clearly, while angiograms out of the contact regions had poor quality. Therefore, we emphasize that our distortion correction method if used in bioimaging should be compatible with larger tissue contact coverage modalities. A balloon sheath design of the catheter is a choice [21,24], which will increase the robustness of the proposed CLG correction method.

Although only 2D endoscopic OCTA imaging results with proximal-end scanning catheters were obtained in our study, there is potential to combine with the additional longitudinal pullback [10,39] to achieve 3D OCTA imaging in the future. However, the problem is that the motion and distortion artifacts will be more serious in 3D OCTA imaging because of pullback. Two aspects can be improved in the current 2D endoscopic OCTA imaging system for high-quality 3D OCTA imaging. First, improving the design of the catheters is necessary, and the balloon sheath design discussed above will serve to stabilize the catheter and suppress the relative motion between the tissue and catheter while the catheter is rapidly rotated and slowly pulled back [23]. Secondly, choosing a suitable scanning pattern will be essential. A helical scanning pattern with high-density sampling can be a choice, where the interval is calculated to be  $\sim 5 \mu\text{m}$  ( $\sim 2.5$  times Nyquist) along the pullback direction [24], and such a small sampling interval enables the assumption of the tissue intensity constant between adjacent frames, which ensures the CLG correction method works in motion artifacts and distortions correction. Therefore, a decorrelation map can be calculated with at least three consecutive corrected OCT frames to suppress background decorrelation noise [24]. In addition, a stepwise raster scanning pattern commonly used in ophthalmology OCT systems may be another choice worth exploring in 3D endoscopic OCTA imaging [40], which enables angiograms extraction from repeated frames with minimal background decorrelation noise. It is possible with the improved proximal-end scanning catheters to acquire 3D angiograms from the cross-sectional CLG-corrected OCT data in the future.

## 5. Conclusions

In this work, we proposed an endoscopic OCTA using a clinical proximal-end scanning catheter with a diameter of 0.9 mm. To suppress artifacts caused by NURD and physiological motion, the CLG method was used in static ROI to calculate the motion displacements in circumferential and radial directions, and the averaged motion vectors of one A-line were used to bicubic-spline-resample the OCT structure. The IDa-OCTA angiograms of the phantom and human finger nailfold were acquired, demonstrating the performance of the distortion correction method. Endoscopic OCTA imaging enables rapid visualization of subsurface structures and vasculature in a depth-resolved manner. These unique features of the endoscopic OCTA have potential to improve the early diagnostic capability of inner organs.

**Author Contributions:** Conceptualization, L.Y. and P.L.; methodology, L.Y. and P.L.; software, L.Y. and P.L.; validation, L.Y., Y.Z. and P.L.; formal analysis, L.Y., Y.Z. and P.L.; investigation, L.Y. and P.L.; resources, L.Y., Y.Z., K.L., X.Y., X.D., Z.D., P.L.; data curation, L.Y. and P.L.; writing—original draft preparation, L.Y., Y.Z., K.L., X.Y., X.D., Z.D., P.L.; writing—review and editing, L.Y., Y.Z., K.L., X.Y., X.D., Z.D., P.L.; visualization, L.Y., Y.Z., K.L., X.Y., X.D., Z.D., P.L.; supervision, P.L.; project administration, P.L.; funding acquisition, P.L. All authors have read and agreed to the published version of the manuscript.

**Funding:** This research was funded by the National Natural Science Foundation of China (62075189, 62035011, 11974310, 31927801), the Zhejiang Provincial Natural Science Foundation of China (LR19F050002), Zhejiang Lab (2018EB0ZX01), the National Key Research and Development Program of China (2017YFA0700501), and the MOE Frontier Science Center for Brain Science and Brain-Machine Integration, Zhejiang University.

**Institutional Review Board Statement:** This study was conducted in accordance with the Declaration of Helsinki (as revised in 2013), and approved by the Ethics Committee of Zhejiang University (No.: IRB-2021-461).

**Informed Consent Statement:** Informed consent was obtained from all subjects involved in the study.

**Data Availability Statement:** The data presented in this study are available on request from the corresponding author.

**Conflicts of Interest:** The authors declare no conflict of interest.

## References

1. Kumagai, Y.; Toi, M.; Inoue, H. Dynamism of tumour vasculature in the early phase of cancer progression: Outcomes from oesophageal cancer research. *Lancet Oncol.* **2002**, *3*, 604–610. [[CrossRef](#)]
2. Sharma, P.; Bansal, A.; Mathur, S.; Wani, S.; Cherian, R.; McGregor, D.; Higbee, A.; Hall, S.; Weston, A. The utility of a novel narrow band imaging endoscopy system in patients with Barrett’s esophagus. *Gastrointest. Endosc.* **2006**, *64*, 167–175. [[CrossRef](#)] [[PubMed](#)]
3. Wallace, M.; Lauwers, G.Y.; Chen, Y.; Dekker, E.; Fockens, P.; Sharma, P.; Meining, A. Miami classification for probe-based confocal laser endomicroscopy. *Endoscopy* **2011**, *43*, 882–891. [[CrossRef](#)] [[PubMed](#)]
4. Wang, R.K.; Jacques, S.L.; Ma, Z.; Hurst, S.; Hanson, S.R.; Gruber, A. Three dimensional optical angiography. *Opt. Express* **2007**, *15*, 4083–4097. [[CrossRef](#)] [[PubMed](#)]
5. Jia, Y.; Tan, O.; Tokayer, J.; Potsaid, B.; Wang, Y.; Liu, J.J.; Kraus, M.F.; Subhash, H.; Fujimoto, J.G.; Hornegger, J.; et al. Split-spectrum amplitude-decorrelation angiography with optical coherence tomography. *Opt. Express* **2012**, *20*, 4710–4725. [[CrossRef](#)] [[PubMed](#)]
6. Huang, L.; Fu, Y.; Chen, R.; Yang, S.; Qiu, H.; Wu, X.; Zhao, S.; Gu, Y.; Li, P. SNR-adaptive OCT angiography enabled by statistical characterization of intensity and decorrelation with multi-variate time series model. *IEEE Trans. Med. Imaging* **2019**, *38*, 2695–2704. [[CrossRef](#)]
7. Skalet, A.H.; Li, Y.; Lu, C.D.; Jia, Y.; Lee, B.; Husvogt, L.; Maier, A.; Fujimoto, J.G.; Thomas, C.R.; Huang, D. Optical Coherence Tomography Angiography Characteristics of Iris Melanocytic Tumors. *Ophthalmology* **2017**, *124*, 197–204. [[CrossRef](#)]
8. Lu, Y.; Wang, J.C.; Zeng, R.; Nagata, T.; Katz, R.; Mukai, S.; Miller, J.B. Detection of retinal microvascular changes in von Hippel-Lindau disease using optical coherence tomography angiography. *PLoS ONE* **2020**, *15*, e0229213. [[CrossRef](#)]
9. Custo Greig, E.P.; Duker, J.S. Retinal hemangioblastoma vascular detail elucidated on swept source optical coherence tomography angiography. *Am. J. Ophthalmol. Case Rep.* **2021**, *21*, 101005. [[CrossRef](#)]
10. Tsai, T.-H.; Ahsen, O.O.; Lee, H.-C.; Liang, K.; Figueiredo, M.; Tao, Y.K.; Giacomelli, M.G.; Potsaid, B.M.; Jayaraman, V.; Huang, Q.; et al. Endoscopic Optical Coherence Angiography Enables 3-Dimensional Visualization of Subsurface Microvasculature. *Gastroenterology* **2014**, *147*, 1219–1221. [[CrossRef](#)]
11. Lee, H.C.; Ahsen, O.O.; Liang, K.; Wang, Z.; Figueiredo, M.; Giacomelli, M.G.; Potsaid, B.; Huang, Q.; Mashimo, H.; Fujimoto, J.G. Endoscopic optical coherence tomography angiography microvascular features associated with dysplasia in Barrett’s esophagus (with video). *Gastrointest. Endosc.* **2017**, *86*, 476–484.e3. [[CrossRef](#)] [[PubMed](#)]
12. Wurster, L.M.; Shah, R.N.; Placzek, F.; Kretschmer, S.; Niederleithner, M.; Ginner, L.; Ensher, J.; Minneman, M.P.; Hoover, E.E.; Zappe, H.; et al. Endoscopic optical coherence tomography angiography using a forward imaging piezo scanner probe. *J. Biophotonics* **2019**, *12*, e201800382.
13. Yao, L.; Li, H.; Liu, K.; Zhang, Z.; Li, P. Endoscopic optical coherence tomography angiography using inverse SNR-amplitude decorrelation features and electrothermal micro-electro-mechanical system raster scan. *Quant. Imaging Med. Surg.* **2022**, *12*, 3078–3091. [[CrossRef](#)]
14. Gora, M.J.; Suter, M.J.; Tearney, G.J.; Li, X. Endoscopic optical coherence tomography: Technologies and clinical applications [Invited]. *Biomed. Opt. Express* **2017**, *8*, 2405–2444. [[CrossRef](#)] [[PubMed](#)]

15. Tsai, T.H.; Lee, H.C.; Ahsen, O.O.; Liang, K.; Giacomelli, M.G.; Potsaid, B.M.; Tao, Y.K.; Jayaraman, V.; Figueiredo, M.; Huang, Q.; et al. Ultrahigh speed endoscopic optical coherence tomography for gastroenterology. *Biomed. Opt. Express* **2014**, *5*, 4387–4404. [[CrossRef](#)] [[PubMed](#)]
16. Aizu, Y.; Yatagai, T.; Awatsuji, Y.; Matoba, O.; Jayaraman, V.; Wang, Z.; Ahsen, O.O.; Liang, K.; Lee, H.-C.; Fujimoto, J.G. Endoscopic Optical Coherence Tomography and Angiography for Gastroenterology Applications. In *Biomedical Imaging and Sensing Conference*; International Society for Optics and Photonics: Bellingham, WA, USA, 2018; p. 107110A. [[CrossRef](#)]
17. Zhang, J.; Nguyen, T.; Potsaid, B.; Jayaraman, V.; Burgner, C.; Chen, S.; Li, J.; Liang, K.; Cable, A.; Traverso, G.; et al. Multi-MHz MEMS-VCSEL swept-source optical coherence tomography for endoscopic structural and angiographic imaging with miniaturized brushless motor probes. *Biomed. Opt. Express* **2021**, *12*, 2384–2403. [[CrossRef](#)] [[PubMed](#)]
18. Ahsen, O.O.; Lee, H.C.; Giacomelli, M.G.; Wang, Z.; Liang, K.; Tsai, T.H.; Potsaid, B.; Mashimo, H.; Fujimoto, J.G. Correction of rotational distortion for catheter-based en face OCT and OCT angiography. *Opt. Lett.* **2014**, *39*, 5973–5976. [[CrossRef](#)]
19. Liang, K.; Wang, Z.; Ahsen, O.O.; Lee, H.C.; Potsaid, B.M.; Jayaraman, V.; Cable, A.; Mashimo, H.; Li, X.; Fujimoto, J.G. Cycloid scanning for wide field optical coherence tomography endomicroscopy and angiography in vivo. *Optica* **2018**, *5*, 36–43. [[CrossRef](#)]
20. Joseph, S.; Adnan, A.; Subhash, H.M.; Leahy, M.; Adlam, D. Developing cross-correlation as a method for microvessel imaging using clinical intravascular optical coherence tomography systems. *Biomed. Opt. Express* **2015**, *6*, 668–689. [[CrossRef](#)]
21. Nguyen, T.H.; Ahsen, O.O.; Liang, K.; Zhang, J.; Mashimo, H.; Fujimoto, J.G. Correction of circumferential and longitudinal motion distortion in high-speed catheter/endoscope-based optical coherence tomography. *Biomed. Opt. Express* **2021**, *12*, 226–246. [[CrossRef](#)]
22. Joseph, S.; Rousseau, C.; Molly Subhash, H.; Leahy, M.; Adlam, D. Variation in Cross-Correlation as a discriminator for microvessel imaging using clinical intravascular Optical Coherence Tomography systems. *Prog. Biomed. Opt. Imaging-Proc. SPIE* **2014**, *8934*, 181–187. [[CrossRef](#)]
23. Kang, W.; Wang, H.; Wang, Z.; Jenkins, M.W.; Isenberg, G.A.; Chak, A.; Rollins, A.M. Motion artifacts associated with in vivo endoscopic OCT images of the esophagus. *Opt. Express* **2011**, *19*, 20722–20735. [[CrossRef](#)] [[PubMed](#)]
24. Lee, H.C.; Ahsen, O.O.; Liang, K.; Wang, Z.; Cleveland, C.; Booth, L.; Potsaid, B.; Jayaraman, V.; Cable, A.E.; Mashimo, H.; et al. Circumferential optical coherence tomography angiography imaging of the swine esophagus using a micromotor balloon catheter. *Biomed. Opt. Express* **2016**, *7*, 2927–2942. [[CrossRef](#)] [[PubMed](#)]
25. Uribe-Patarroyo, N.; Bouma, B.E. Rotational distortion correction in endoscopic optical coherence tomography based on speckle decorrelation. *Opt. Lett.* **2015**, *40*, 5518–5521. [[CrossRef](#)] [[PubMed](#)]
26. Horn, B.K.P.; Schunck, B.G. Determining optical flow. *Artif. Intell.* **1981**, *17*, 185–203. [[CrossRef](#)]
27. Stein, K.U.; Gonglewski, J.D.; Huebner, C.S. Local motion compensation in image sequences degraded by atmospheric turbulence: A comparative analysis of optical flow vs. block matching methods. In *Proceedings of the Optics in Atmospheric Propagation and Adaptive Systems XIX*, Edinburgh, UK, 28–29 September 2016.
28. Sun, C.; Nolte, F.; Cheng, K.H.Y.; Vuong, B.; Lee, K.K.C.; Standish, B.A.; Courtney, B.; Marotta, T.R.; Mariampillai, A.; Yang, V.X.D. In vivo feasibility of endovascular Doppler optical coherence tomography. *Biomed. Opt. Express* **2012**, *3*, 2600–2610. [[CrossRef](#)] [[PubMed](#)]
29. Lucas, B.; Kanade, T. An Iterative Image Registration Technique with an Application to Stereo Vision. In *Proceedings of the 7th International Joint Conference on Artificial Intelligence*, Vancouver, BC, Canada, 24–28 August 1981.
30. Brox, T.; Bruhn, A.; Papenberger, N.; Weickert, J. *High Accuracy Optical Flow Estimation Based on a Theory for Warping*; Springer: Berlin/Heidelberg, Germany, 2004; pp. 25–36.
31. Bruhn, A.; Weickert, J.; Schnörr, C. Lucas/Kanade Meets Horn/Schunck: Combining Local and Global Optic Flow Methods. *IJCV* **2005**, *61*, 211–231. [[CrossRef](#)]
32. Moshaei-Nezhad, Y.; Müller, J.; Schnabel, C.; Kirsch, M.; Tetzlaff, R. A robust optical flow motion estimation and correction method for IRT imaging in brain surgery. *Quant. InfraRed Thermogr. J.* **2020**, *18*, 226–251. [[CrossRef](#)]
33. Gao, S.S.; Jia, Y.; Liu, L.; Zhang, M.; Takusagawa, H.L.; Morrison, J.C.; Huang, D. Compensation for Reflectance Variation in Vessel Density Quantification by Optical Coherence Tomography Angiography. *Investig. Ophthalmol. Visual Sci.* **2016**, *57*, 4485–4492. [[CrossRef](#)]
34. Xu, J.; Wei, W.; Song, S.; Qi, X.; Wang, R.K. Scalable wide-field optical coherence tomography-based angiography for in vivo imaging applications. *Biomed. Opt. Express* **2016**, *7*, 1905–1919. [[CrossRef](#)]
35. Lagemann, C.; Lagemann, K.; Mukherjee, S.; Schröder, W. Deep recurrent optical flow learning for particle image velocimetry data. *Nat. Mach. Intell.* **2021**, *3*, 641–651. [[CrossRef](#)]
36. Kim, H.J.; Kim, M.H.; Lee, S.K.; Yoo, K.S.; Seo, D.W.; Min, Y.I. Tumor vessel: A valuable cholangioscopic clue of malignant biliary stricture. *Gastrointest. Endosc.* **2000**, *52*, 635–638. [[CrossRef](#)] [[PubMed](#)]
37. Jung, W.; Benalcazar, W.; Ahmad, A.; Sharma, U.; Tu, H.; Boppart, S.A. Numerical analysis of gradient index lens-based optical coherence tomography imaging probes. *J. Biomed. Opt.* **2010**, *15*, 066027. [[CrossRef](#)] [[PubMed](#)]
38. Xi, J.; Huo, L.; Wu, Y.; Cobb, M.J.; Hwang, J.H.; Li, X. High-resolution OCT balloon imaging catheter with astigmatism correction. *Opt. Lett.* **2009**, *34*, 1943–1945. [[CrossRef](#)]

- 
39. Li, J.; de Groot, M.; Helderma, F.; Mo, J.; Daniels, J.M.A.; Grünberg, K.; Sutedja, T.G.; de Boer, J.F. High speed miniature motorized endoscopic probe for optical frequency domain imaging. *Opt. Express* **2012**, *20*, 24132–24138. [[CrossRef](#)]
  40. Liu, K.; Zhu, T.; Yao, L.; Zhang, Z.; Li, H.; Ye, J.; Li, P. Noninvasive OCT angiography-based blood attenuation measurements correlate with blood glucose level in the mouse retina. *Biomed. Opt. Express* **2021**, *12*, 4680–4688. [[CrossRef](#)]